Elementary Mechanisms Producing Facilitation of $Ca_V2.1$ (P/Q-type) Channels

Dipayan Chaudhuri,[1] John B. Issa,[2] and David T. Yue[1,2]

[1]Department of Neuroscience and [2]Department of Biomedical Engineering, The Johns Hopkins University School of Medicine, Baltimore, MD 21205

The regulation of $Ca_V2.1$ (P/Q-type) channels by calmodulin (CaM) showcases the powerful Ca^{2+} decoding capabilities of CaM in complex with the family of Ca_V1-2 Ca^{2+} channels. Throughout this family, CaM does not simply exert a binary on/off regulatory effect; rather, Ca^{2+} binding to either the C- or N-terminal lobe of CaM alone can selectively trigger a distinct form of channel modulation. Additionally, Ca^{2+} binding to the C-terminal lobe triggers regulation that appears preferentially responsive to local Ca^{2+} influx through the channel to which CaM is attached (local Ca^{2+} preference), whereas Ca^{2+} binding to the N-terminal lobe triggers modulation that favors activation via Ca^{2+} entry through channels at a distance (global Ca^{2+} preference). $Ca_V2.1$ channels fully exemplify these features; Ca^{2+} binding to the C-terminal lobe induces Ca^{2+}-dependent facilitation of opening (CDF), whereas the N-terminal lobe yields Ca^{2+}-dependent inactivation of opening (CDI). In mitigation of these interesting indications, support for this local/global Ca^{2+} selectivity has been based upon indirect inferences from macroscopic recordings of numerous channels. Nagging uncertainty has also remained as to whether CDF represents a relief of basal inhibition of channel open probability (P_o) in the presence of external Ca^{2+}, or an actual enhancement of P_o over a normal baseline seen with Ba^{2+} as the charge carrier. To address these issues, we undertake the first extensive single-channel analysis of $Ca_V2.1$ channels with Ca^{2+} as charge carrier. A key outcome is that CDF persists at this level, while CDI is entirely lacking. This result directly upholds the local/global Ca^{2+} preference of the lobes of CaM, because only a local (but not global) Ca^{2+} signal is here present. Furthermore, direct single-channel determinations of P_o and kinetic simulations demonstrate that CDF represents a genuine enhancement of open probability, without appreciable change of activation kinetics. This enhanced-opening mechanism suggests that the CDF evoked during action-potential trains would produce not only larger, but longer-lasting Ca^{2+} responses, an outcome with potential ramifications for short-term synaptic plasticity.

The Journal of General Physiology

INTRODUCTION

The regulation of $Ca_V2.1$ (P/Q-type) channels by calmodulin (CaM) holds special fascination for neurobiologists and ion channel biophysicists alike. As these channels represent the dominant trigger of neurotransmitter release in the central nervous system (Wheeler et al., 1994; Dunlap et al., 1995; Wheeler and Tsien, 1999), their CaM-mediated regulation is considered a potentially important mechanism for short-term synaptic plasticity (Borst and Sakmann, 1998; Cuttle et al., 1998; Xu and Wu, 2005), and thereby the neurocomputation of neural networks (Tsodyks and Markram, 1997; Tsodyks et al., 1998; Zucker and Regehr, 2002; Abbott and Regehr, 2004). From the channel biophysical viewpoint, this modulatory system prominently showcases the powerful Ca^{2+} decoding capabilities of CaM in complex with Ca_V1-2 voltage-gated Ca^{2+} channels. There are three notable distinctives of this system. First, CaM in its Ca^{2+}-free form (apoCaM) is already preassociated with $Ca_V2.1$ channels (DeMaria et al., 2001; Erickson et al., 2001); CaM is therefore poised to respond to Ca^{2+} elevations as a resident Ca^{2+} sensor. Second, subsequent Ca^{2+} binding to this resident CaM does not simply exert a binary on/off regulatory effect on $Ca_V2.1$ channels. Rather Ca^{2+} binding to the C-terminal lobe of CaM selectively induces conformational changes that yield a facilitation of channel opening occurring over tens of milliseconds (Ca^{2+}-dependent facilitation [CDF]), whereas Ca^{2+} binding to the N-terminal lobe of CaM preferentially triggers alternate molecular changes that inactivate channel opening over the course of hundreds of milliseconds (Ca^{2+}-dependent inactivation [CDI]) (Lee et al., 1999; DeMaria et al., 2001; Lee et al., 2003; Chaudhuri et al., 2004). This CaM lobe–specific signaling represents an extreme form of the bipartitioning capabilities first observed in *Paramecia* (Kink et al., 1990). Third, though the two lobes of preassociated CaM are no doubt contained within the cytoplasmic nanodomain of channels (Augustine et al., 2003), they nonetheless seem to respond to different Ca^{2+} signal

Correspondence to David T. Yue: dyue@bme.jhu.edu

D. Chaudhuri's present address is Department of Medicine, University of California, San Francisco, CA 94143.

Abbreviations used in this paper: APW, action-potential waveform; CaM, calmodulin; CDF, Ca^{2+}-dependent facilitation of opening; CDI, Ca^{2+}-dependent inactivation of opening; VDI, voltage-dependent inactivation process.

components embedded within the fluctuations of Ca^{2+} concentration within this same nanodomain (Liang et al., 2003). Ca^{2+} binding to the C-terminal lobe of CaM triggers regulatory processes (e.g., CDF in $Ca_V2.1$) that seem to respond preferentially to intense, spike-like Ca^{2+} fluctuations driven by local Ca^{2+} influx through the channel to which resident CaM is attached (local Ca^{2+} preference) (Lee et al., 2000; DeMaria et al., 2001; Soong et al., 2002; Chaudhuri et al., 2004; Chaudhuri et al., 2005). By contrast, Ca^{2+} binding to the N-terminal lobe activates modulatory processes (e.g., CDI in $Ca_V2.1$) that appear selective for smaller but long-lasting Ca^{2+} components reflective of Ca^{2+} entry through multiple other Ca^{2+} channels at a distance from the resident CaM (global Ca^{2+} preference). Though the precise form of modulation (CDF or CDI) produced by a particular lobe of CaM may vary in different types of Ca^{2+} channels, the overall preference of the C-terminal lobe of preassociated CaM for local Ca^{2+}, and of the N-terminal lobe for global Ca^{2+}, appears to hold true across the family of Ca_V1-2 channels (Evans and Zamponi, 2006).

Ongoing biological research is beginning to reveal the impact of CaM/Ca^{2+} channel regulation on cardiac (Alseikhan et al., 2002) and neuronal excitability (Chaudhuri et al., 2004; Chaudhuri et al., 2005; Yang et al., 2006). This study focuses instead upon critical gaps in our understanding of the mechanisms underlying CaM regulation of $Ca_V2.1$. A first key uncertainty concerns the suggested selectivity of CaM/channel regulation for spatially different sources of Ca^{2+} influx. The data in support of this selectivity have thus far been indirect and based upon inferences drawn from macroscopic currents recordings from numerous channels. Whether this intriguing design principle actually exists could be tested directly at the single-channel level, where the local Ca^{2+} signal is present, but the global Ca^{2+} signal must be lacking by definition. A second critical unknown is whether $Ca_V2.1$ CDF represents a derepression of channel open probability (P_o), or an actual enhancement of P_o over a normal baseline level seen without Ca^{2+}. Though either scenario would cohere with the macroscopic profile of CDF, direct determination of P_o by single-channel recording would definitively adjudicate this ambiguity. Thus far, however, single-channel data for $Ca_V2.1$ channels have been limited primarily to those obtained with Ba^{2+} as the charge carrier (Dove et al., 1998; Hans et al., 1999; Colecraft et al., 2001; Tottene et al., 2002; Fellin et al., 2004; Luvisetto et al., 2004; Tottene et al., 2005), where experimental resolution of signals is aided by the amplification of unitary current size (i) compared to that seen with the physiological charge carrier Ca^{2+} (Tottene et al., 2002). Rapid millisecond openings of unitary $Ca_V2.1$ Ca^{2+} currents are estimated to produce currents of only 300–400 femptoamps in amplitude (even with ~100 mM Ca^{2+} as charge carrier); this challenging regime is at the cusp of practical experimental resolution by patch clamp.

Nonetheless, to address these and other open questions, we here undertake the first extensive single-channel analysis of $Ca_V2.1$ channels with Ca^{2+} as the charge carrier. This analysis provides direct support for the proposed spatial Ca^{2+} selectivity of the C- versus N-terminal lobes of CaM. Furthermore, extensive kinetic analysis strongly supports a genuine enhancement of P_o as the underlying basis of CDF. This outcome raises novel perspectives on the potential impact of CDF at presynaptic termini.

MATERIALS AND METHODS

Cell Culture and Transient Transfection

HEK293 cells were cultured and maintained as previously described (Brody et al., 1997). To express recombinant P/Q-type channels, HEK293 cells were cotransfected with plasmids encoding the human α_{1A} pore-forming subunit (Soong et al., 2002); the β_{2a} (Perez-Reyes et al., 1992) and $\alpha_2\delta$ (Tomlinson et al., 1993) accessory subunits; and finally the RSV T antigen. Transfection was accomplished with a calcium phosphate protocol (Dhallan et al., 1990). The β_{2a} subunit reduces voltage inactivation (Patil et al., 1998), allowing simpler examination of Ca^{2+}-dependent processes in relative isolation. The plasmid encoding the β_{2a} subunit also encoded a GFP sequence following an internal ribosomal entry site, so as to identify successfully transfected HEK293 cells by fluorescence. The RSV T antigen permits plasmid replication in HEK293 cells, thereby enhancing expression. The human α_{1A} ($\alpha_1$2.1) clone used was either an "EF_a" splice variant, or an "EF_b" splice variant. The exact splice background of these constructs were as follows (Soong et al., 2002; Chaudhuri et al., 2004): Δ10A (+G); $16^+/17^+$; 17 (−VEA), −31*(−NP); 37a (EF_a) or 37b (EF_b); $43^+/44^-$; 47+.

Electrophysiology

2–4 d after transfection, we performed room temperature electrophysiological recordings in one of two configurations, using an Axopatch 200A amplifier (Axon Instruments).

For whole-cell recordings, the bath solution contained 150 mM tetraethylammonium methanesulfonate (TEA-$MeSO_3$), either 5 mM $CaCl_2$ or $BaCl_2$, 1 mM $MgCl_2$, and 10 mM HEPES (adjusted to pH 7.4 with TEA-OH). The internal solution contained 135 mM cesium methanesulfonate (Cs-$MeSO_3$), 5 mM CsCl, 0.5 mM EGTA, 1 mM $MgCl_2$, 10 mM HEPES, and freshly added 4 mM MgATP (pH 7.4, adjusted with CsOH). Electrodes were pulled with borosilicate glass capillaries (World Precision Instruments, MTW 150-F4), resulting in 1–3 MΩ resistances, before series resistance compensation of 75%. Voltage pulses were applied at 30–90-s intervals. Currents were filtered at 2 kHz for routine rectangular step protocols, and at 5 kHz for action potential (AP) trains and tail current measurements (4-pole Bessel), and digitized at 4–5× higher frequencies. Leak and capacitance transients were subtracted by a P/8 protocol. AP voltage templates were based on recordings from the Calyx of Held (Borst et al., 1995; Patil et al., 1998).

For cell-attached single-channel currents, the bath contained 132 mM K-glutamate, 5 mM KCl, 5 mM NaCl, 3 mM $MgCl_2$, 2 mM EGTA, 10 mM glucose, and 20 mM HEPES (pH 7.4, adjusted with KOH). This solution zeroed the membrane potential. The pipette solution contained either 90 mM $BaCl_2$ or 100 mM $CaCl_2$, 20 mM TEA-$MeSO_3$, and 10 mM HEPES (pH 7.4, adjusted with

TEA-OH). 5–20 MΩ patch pipettes were fashioned from ultra-thick-walled (2-mm outer diameter, 1.16-mm inner diameter) borosilicate glass (BF200-116-10, Sutter Instruments), and coated with Sylgard. This thick-walled glass minimized electrical noise. Voltage pulses were applied at a repetition interval of 6 s; data were sampled at 50-μs intervals and filtered at 2 kHz for Ba^{2+} currents and 1.25 kHz for Ca^{2+} currents (−3 dB, 4-pole Bessel).

Single-Channel Analysis

Smooth functions were fitted to leak and capacity transients (P/8 protocol), and these were subtracted from single-channel records in a semiautomatic manner using custom software written in MATLAB (MathWorks). These records were then converted to idealized format using half-height criteria. Most patches contained one to two channels, with an approximately even distribution. The number of channels was judged from the maximum number of simultaneous openings (Horn, 1991). Single-channel statistics were calculated as described previously (Imredy and Yue, 1994; Patil et al., 1996; Colecraft et al., 2001). In brief, ensemble averages were normalized by the unitary current amplitude i and the number of channels N, yielding simple open probability P_o. The first latency distribution function FL, defined as the probability that a first opening occurred before time t in a voltage pulse, was calculated as

$$FL = 1 - \left(1 - FL_N\right)^{1/N},$$

where FL_N is the apparent first latency function for a patch containing N channels. The conditional open probability function $P_{oo}(t)$ is defined as the probability that a channel is found open with a delay t after a channel first opens. For patches with one channel, this is calculated by time-shifting idealized records with a first opening in the first 100 ms of the test pulse, such that all first openings occur at $t = 0$. All such time-shifted records are then ensemble averaged and divided by i. Records with first openings after the first 100 ms of the pulse were excluded from analysis, so that the calculated $P_{oo}(t)$ would be reliable for at least 100 ms after the instant of first opening. Recall that the test pulse duration was 200–250 ms; hence, inclusion of records with first openings after the 100-ms time point would produce "edge effects" in the calculation of $P_{oo}(t)$. In practice, the frequency of traces with first openings occurring after the 100-ms time point was exceedingly low (see FL functions in Figs. 5 and 6). With more than one channel ($N > 1$), the procedure was subtly modified as previously developed (Imredy and Yue, 1992; Patil et al., 1996; Colecraft et al., 2001). The basic insight for the procedure is to appropriately conceptualize the conditional expectation value for unitary current records wherein the first observed opening occurs at time t_j within the test pulse. This representation is

$$E_i(t \mid \text{1st observed opening at } t_j) =$$
$$i \cdot P_{oo}(t \mid \text{a channel 1st opens at } t_j) + (N-1) \cdot i \cdot P_o(t \mid \overline{\text{O}} \text{ during } f),$$

where $E_i(t|\text{1st observed opening at } t_j)$ is the conditional expectation in question; $P_{oo}(t|\text{a channel 1st opens at } t_j)$ is the conditional P_o for a single channel at time t given that this channel first opens at time t_j; and $P_o(t|\overline{\text{O}}$ up to $t_j)$ is the conditional open probability of one of the channels given that none of the N channels open before time t_j in the test pulse. Accordingly, $P_{oo}(t)$ could be calculated as follows. For each record r (with first observed opening at time t_j), we initially compensated this record to produce r_{adj} as given by

$$r_{adj} = r - (N-1) \cdot i \cdot P_o(t \mid \overline{\text{O}} \text{ up to } t_j)$$

where $i \cdot P_o(t|\overline{\text{O}}$ up to $t_j)$ was calculated by (a) selecting all records lacking openings before time t_j in the test pulse, (b) averaging all of these selected records, and (c) normalizing this average by N. This adjusted record r_{adj} was subsequently time shifted (by t_j) such that its first opening then appears at $t = 0$. We ensemble averaged all such time-shifted records, and divided by i, yielding $P_{oo}(t)$ for a single channel. Regardless of the number of channels in a patch, open times were determined from all openings without stacking to a second or higher level. In multichannel patches, this procedure would in principle underestimate longer openings. However, due to the low open probability of $Ca_v2.1$ in our experiments, such stacked openings were comparatively rare, and thus our open times would be insignificantly impacted.

Enhanced-opening Mechanism Simulations

The kinetic simulations in Fig. 8 were performed by numerically solving the system of differential equations that describes the enhanced-opening mechanism. Custom-written MATLAB software was used for this purpose, using standard algorithms (Patil et al., 1996) and the rate-constant parameters shown in Fig. 8. Two features merit further elaboration. First, a small fraction (<10%) of single-channel sweeps failed to exhibit any openings ("blank" sweeps). This was probably due to a small degree of cumulative voltage-dependent inactivation at the onset of test-pulse depolarizations, owing to the comparatively short interval between depolarizations in single-channel experiments (6 s). This short interval was required to obtain a sufficient number of sweeps within the typical lifetime of a cell-attached recording. By contrast, whole-cell recordings employ depolarizations every 30–90 s. To account for such cumulative inactivation in the simulation of experimentally determined P_o and FL, the sum of all state probabilities was adjusted downward from unity, to the value of the corresponding experimentally determined FL function at t = 100–150 ms (near the plateau). These values were 0.988 (Fig. 8 A), 0.984 (Fig. 8 B), and 0.916 (Fig. 8, C and D). Second, to explain the detailed kinetics of the P_{oo} function in Fig. 8 D, the transition from normal to facilitated modes of gating could not be modeled as a single-step transition. Instead, we adopted the simplest form of transition that depends upon the activation of multiple, independent homologous domains. More complex transitions of this form could be valid, but absent more detailed data, we have retained the simplest form of such schemes. It is assumed that while the normal mode channel is open and driving high nanodomain Ca^{2+} concentrations, Ca^{2+} binding to CaM is in rapid equilibrium with this high Ca^{2+}, yielding B as the a fractional Ca^{2+} occupancy of CaM binding while the channel is open. When the channel is closed, Ca^{2+} is presumed to rapidly unbind from CaM. Each of four homologous domains can become permissive for facilitation (by rate constant α) only when Ca^{2+} is bound to CaM; likewise, domains can only return to the nonpermissive state (by rate constant β) when Ca^{2+} is bound to CaM. Thus, the transitions between permissive (E) and nonpermissive (D) configurations of a homologous domain are given by the reaction scheme

$$D \underset{\beta \cdot B \cdot P_{o\,|\,\text{normal}}}{\overset{\alpha \cdot B \cdot P_{o\,|\,\text{normal}}}{\rightleftharpoons}} E,$$

where $P_{o\,|\,\text{normal}}$ is the open probability given that a channel is in the normal mode of gating. Presuming that all four homologous domains of the channel are equivalent and independent, and that they must all be permissive for the channel to become functionally facilitated (according to rate constant γ), the net transition rate from normal to facilitated modes of gating becomes $\gamma \cdot \varepsilon^4$, where ε is the probability of a homologous domain residing in the E conformation. For the simulation in Fig. 8 D, α = 2.2 ms^{-1}, β = 0.01 ms^{-1}, and γ = 15 ms^{-1}.

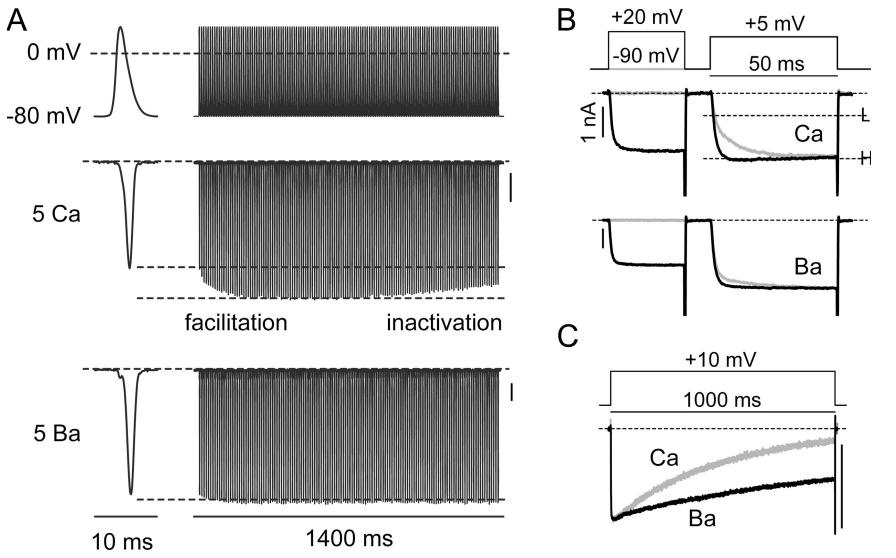

Figure 1. Ca^{2+} regulation of $Ca_V2.1$ (P/Q-type) Ca^{2+} channels, as seen from macroscopic currents. Currents are from HEK293 cells transfected with recombinant P/Q-type channels ($\alpha_{1A}/\beta_{2a}/\alpha_2\delta$), here and throughout. (A) Evidence of Ca^{2+} regulation during stimulation by action-potential waveforms (APW). Top, 100-Hz APW train, with APWs derived from action potentials recorded in the calyx of Held (Borst et al., 1995; Patil et al., 1998). The single APW on the extreme left is displayed with an expanded timebase, compared with APWs on the right. Middle, corresponding evoked Ca^{2+} currents. Over the first several stimuli, Ca^{2+} currents increase in amplitude, according to a Ca^{2+}-dependent facilitation (CDF) process. With continued repetitive stimulation, the current amplitudes decline by a Ca^{2+}-dependent inactivation (CDI) process. The first response is reproduced on the far left, using a fast time base. Bottom, Ba^{2+} currents evoked in the same cell by the identical APW stimuli. Little facilitation or inactivation is apparent. Vertical bars, 1 nA. (B) CDF as characterized by a rectangular voltage-pulse protocol. Top, voltage pulse paradigms. To resolve CDF while minimizing CDI, test pulse depolarizations (to +5 mV) are comparatively short (50 ms). Test pulse depolarization is delivered either without a preceding voltage prepulse (gray segment), or with a brief voltage prepulse (to +20 mV). Middle, corresponding evoked Ca^{2+} currents. Without a prepulse, test pulse depolarization initially evokes rapid activation to a lower level, marked L. Following this, Ca^{2+} current (gray trace) slowly increases to a higher level H, according to CDF. When test pulse depolarization follows a voltage prepulse, Ca^{2+} current (black trace) activates immediately to the higher level, because channels have already undergone CDF in the prior prepulse. Bottom, Ba^{2+} currents evoked identically in the same cell show little indication of facilitation. Unless noted otherwise, the scale bar pertains to Ca^{2+} currents here and subsequently throughout, while Ba^{2+} currents are scaled downward by 2–3× to optimize visual comparison of kinetics. (C) Prolonged 1-s depolarization to near the peak of *I-V* relations (+10 mV) produces faster decay of Ca^{2+} versus Ba^{2+} current, indicative of CDI.

RESULTS

Macroscopic View of Ca^{2+}-dependent Facilitation and Inactivation

Fig. 1 reviews the overall features of $Ca_V2.1$ channel regulation by Ca^{2+}, as viewed at the level of macroscopic currents. This overview sets the stage for the ensuing focus of this study, the single-channel dissection of mechanisms underlying such regulation. During stimulation of whole-cell recombinant currents by a train of action potential waveforms (Fig. 1 A, top), the likely impact of such Ca^{2+} regulation on physiological responses becomes apparent (Fig. 1 A, middle); the initial increase in peak currents over the first several spikes reflects a Ca^{2+}-dependent facilitation process (CDF); and the subsequent decline over hundreds of milliseconds results from a Ca^{2+}-dependent inactivation process (CDI) (Lee et al., 1999; DeMaria et al., 2001). That these processes are genuinely Ca^{2+} dependent (versus voltage dependent) can be demonstrated by substituting Ba^{2+} for Ca^{2+} as the charge carrier (Fig. 1 A, bottom), whereupon peak currents remain essentially stable during an identical train. As both CDF and CDI are triggered by calmodulin (CaM) (Lee et al., 1999; DeMaria et al., 2001), the absence of regulation with Ba^{2+} fits nicely with the high Ca^{2+} over Ba^{2+} selectivity of CaM (Chao et al., 1984).

To conveniently quantify CDF and CDI, we have used rectangular voltage pulse protocols to isolate each process (DeMaria et al., 2001; Chaudhuri et al., 2004). For the more rapid process of CDF, we emphasize comparatively short test pulse depolarizations of ~50 ms (Fig. 1 B, top), a duration short enough to minimize the presence of CDI. When a test pulse is delivered in isolation, Ca^{2+} currents facilitate, as seen from a slow phase of activation (Fig. 1 B, middle, gray trace, from level L to H). Conversely, when channels become facilitated by Ca^{2+} entry during a voltage prepulse, only a rapidly activating current can be seen during the subsequent test pulse (Fig. 1 B, middle, black trace). These clear prepulse-dependent changes in both the amplitude and kinetics of test pulse currents serve as a robust measure of CDF. Consistent with this viewpoint, these changes in test pulse currents are largely absent with Ba^{2+} as charge carrier (Fig. 1 B, bottom). For the slower form of Ca^{2+}-dependent regulation (CDI), we focus upon longer step depolarizations (~1,000 ms) that permit substantial CDI to develop (Fig. 1 C), as evident from the considerably faster decay of Ca^{2+} (gray trace) versus Ba^{2+} currents (black trace). It is worth emphasizing that the CDF events described previously are still present in this Ca^{2+} trace, but are compressed within the first ~50 ms of the 1,000-ms record. Also important, the slow decay

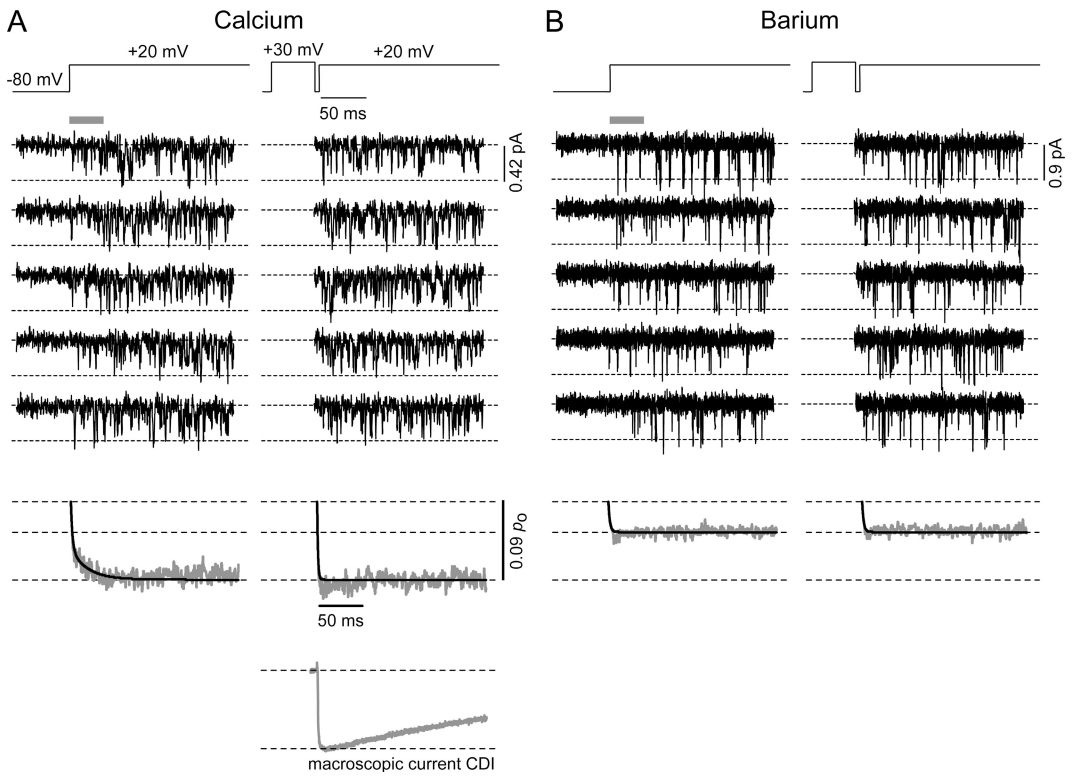

Figure 2. Single P/Q-type channels exhibit CDF, but not CDI. (A) Unitary Ca^{2+} currents during modified voltage prepulse protocol. Top, test pulse depolarizations (+20 mV) without (left) and with (right) a voltage prepulse (30 mV). Middle, single-channel records from an exemplar patch containing one channel. Dashed lines indicate the closed (top, at zero level) and open (bottom) levels of unitary current. Gray rectangle signifies period during which a sparser pattern of gating predominates. Bottom, ensemble average currents after normalization to represent P_o (gray traces), as averaged from $n = 5$ patches. Smooth black curves are fitted by eye. Upper dashed line indicates zero-current level. Middle and lower dashed lines are analogous to L and H levels in Fig. 1 B. Traces show hallmarks of CDF, as present in macroscopic data (Fig. 2 B). Extreme bottom, exemplar whole-cell Ca^{2+} current evoked by +10-mV depolarization, illustrating clearly detectable CDI over the time period observed in single-channel recordings. Absence of such decay in ensemble average currents indicates lack of CDI at the single-channel level. (B) Unitary Ba^{2+} currents observed under an identical protocol; identical format as in A. Middle, exemplar single-channel records from a patch containing one P/Q-type channel. Calibration bar identical to that in A. Bottom, ensemble average currents normalized to P_o, averaged from $n = 5$ patches. Note the absence of a sparser pattern of gating during the corresponding period denoted by a gray rectangle.

of Ba^{2+} current reflects a slower and distinct voltage-dependent inactivation process (VDI) (Patil et al., 1998; Jones et al., 1999; Alseikhan et al., 2002; Stotz et al., 2004), whereas the large acceleration of current decay seen with Ca^{2+} results from the CDI process. Hence, the large difference in Ca^{2+} versus Ba^{2+} current decay over hundreds of milliseconds signals the presence of CDI.

Such macroscopic indications of CDF and CDI have yielded considerable qualitative information regarding these modulatory processes (Lee et al., 1999, 2000, 2003; DeMaria et al., 2001; Soong et al., 2002; Chaudhuri et al., 2004, 2005). Nonetheless, this type of information has left unresolved several fundamental issues in regard to the elementary mechanisms that underlie these regulatory systems.

Are CDF and CDI Present at the Single-Channel Level?

A first salient question regards the purported selectivity of CaM/channel regulation for spatially different sources of Ca^{2+} influx (DeMaria et al., 2001; Liang et al., 2003). Such selectivity could be tested directly at the single-channel level, where only the local (but not global) Ca^{2+} signal is present by definition. Accordingly, if this principle holds true, a single $Ca_V2.1$ channel should exhibit strong CDF, but weak or absent CDI. A second open issue is whether $Ca_V2.1$ CDF represents a derepression of channel open probability (P_o), or a true elevation of P_o. Though either case would accord with macroscopic CDF behavior (Fig. 1 B), unequivocal single-channel measurement of P_o would cleanly resolve the uncertainty.

Accordingly, we explicitly resolved unitary Ca^{2+} currents of single recombinant $Ca_V2.1$ channels. The prepulse protocol here (Fig. 2 A, top) mirrors that described for characterization of macroscopic CDF (Fig. 1 B), except that the test pulse duration is elongated (250 ms), so as to permit detection of both CDF and CDI, if present. Inspection of the single-channel records

(Fig. 2 A, middle) readily reveals stochastic millisecond gating, with small unitary currents of $i \sim 0.4$ pA. The ensemble average of such activity (Fig. 2 A, bottom, from $n = 5$ patches) clearly resolves prepulse-dependent changes that are characteristic of robust CDF. Specifically, in the absence of a prepulse, channels initially feature rapid opening to a low $P_o \sim 0.04$ (Fig. 2 A, bottom left), followed by a slow transition to a higher $P_o \sim 0.09$. However, after prepulse depolarization, channels open immediately to the higher $P_o \sim 0.09$ (Fig. 2 A, bottom right). The overall similarity to macroscopic CDF events is unmistakable (compare Fig. 1 B, middle). By contrast, CDI is absent in these same patches; once achieved, the $P_o \sim 0.09$ is essentially maintained for the entire duration of the 250-ms stimulus (Fig. 2 A, bottom, left and right). For reference, a comparable macroscopic current record exhibits an unmistakable decline over the same time frame (Fig. 2 A, far bottom right). These results directly demonstrate that CaM-dependent processes, as triggered by the C- and N-terminal lobes of CaM, are indeed differentially sensitive to local versus global Ca^{2+} signals.

The direct resolution of P_o also enables us to determine whether CDF merely relieves an initial suppression of basal P_o, or actually boosts P_o over a standard level. To distinguish between these contrasting scenarios, we determined the reference P_o seen with Ba^{2+} as the charge carrier (Fig. 2 B) Since CDF should be absent with Ba^{2+}, the P_o determined here would provide a baseline against which to judge the actions of CDF. Fig. 2 B shows the single-channel activity with Ba^{2+} as charge carrier (middle), evoked with a directly comparable prepulse protocol (top). Unitary current amplitudes are larger ($i \sim 0.9$ pA), and the ensemble averages (bottom, $n = 5$ patches) are identical regardless of a prepulse (Colecraft et al., 2001), confirming the absence of appreciable facilitation. More importantly, the basal P_o reaches ~ 0.04, which is clearly smaller than the Ca^{2+}-facilitated level (compare Fig. 2 A, bottom). Hence, CDF reflects an actual boost in P_o compared with the basal state, rather than derepression of an initially inhibited configuration. Further evidence that Ba^{2+} currents represent a bona fide reference baseline for Ca^{2+} activity is presented later in Fig. 6.

Contrasting CDF Mechanisms: Enhanced Steady-State Opening versus Accelerated Activation

Beyond the fundamental concerns of spatial Ca^{2+} selectivity of CDF versus CDI, and genuine enhancement of P_o by CDF, more in-depth analysis of the single-channel activity (Fig. 2, A and B, middle) could reveal the explicit gating mechanism that underlies the enhancement of P_o. To focus this analysis, we first articulate the two alternative gating mechanisms that could potentially explain CDF (Fig. 3 A). The enhanced opening hypothesis predicts that nonfacilitated channels open into a "normal" mode of gating, characterized by a lower steady-state P_o as seen with Ba^{2+} (Fig. 3 A, left, white states). CDF then results from a CaM-mediated transition to a 'facilitated' mode of gating, featuring a higher steady-state P_o (Fig. 3 A, left, gray states). In Fig. 2 B (left), cartoons illustrate the single-channel patterns corresponding to this proposed mechanism. Without a prepulse (top), a channel opens without much delay, but initially shows the sparser opening pattern of the normal mode. Upon a discrete transition to the enhanced opening mode (top, arrow), the channel adopts a more active opening pattern. After a prepulse (bottom), a channel often starts the ensuing test pulse within the facilitated opening mode. Single-channel activity thereby shows rapid opening directly into the enhanced-opening pattern, which is maintained throughout the test pulse. By contrast, the accelerated activation hypothesis (Fig. 3 A, right) predicts that channels in the facilitated mode first open faster than those in the normal mode, but that channels in either mode maintain similar to identical open probabilities subsequent to first opening (Fig. 3, A and B, right). Mechanisms of this type have been proposed to explain CDF as observed in native P-type Ca^{2+} channel in the calyx of Held (Borst and Sakmann, 1998). Fig. 3 B emphasizes how these different single-channel gating properties would nonetheless elaborate macroscopic currents with closely similar profiles. Moreover, a mixture of these two mechanisms could also support the same macroscopic behavior.

With this view of potential gating schemes in mind, we devise customized means of determining the extent to which each mechanism underlies CDF. Protocols and analysis at both the whole-cell and single-channel levels can provide independent lines of evidence favoring either or both mechanisms, as follows.

Macroscopic Tail Current Analysis of CDF

A first strategy to elucidate the underlying gating mechanisms for CDF concerns whole-cell tail current protocols, which would produce voltage-dependent activation curves as hypothesized in Fig. 3 C. In this protocol, currents are activated by a brief (20-ms) voltage step to a variable potential (V_{step}), followed by repolarization to an invariant tail potential (V_{tail}). Given this setup, rapidly decaying "tail currents" will be produced during the repolarization, the peak amplitude of which (I_{tail}) will be given by

$$I_{tail} = N \cdot P_o(V_{step}) \cdot g \cdot (V_{tail} - V_{rev}),$$

where N is the number of channels in the cell, $P_o(V_{step})$ is the open probability reached at the end of the 20-ms voltage step, g is the single-channel conductance, and V_{rev} is the reversal potential. Because all factors are held constant, except for V_{step}, normalization of the tail current

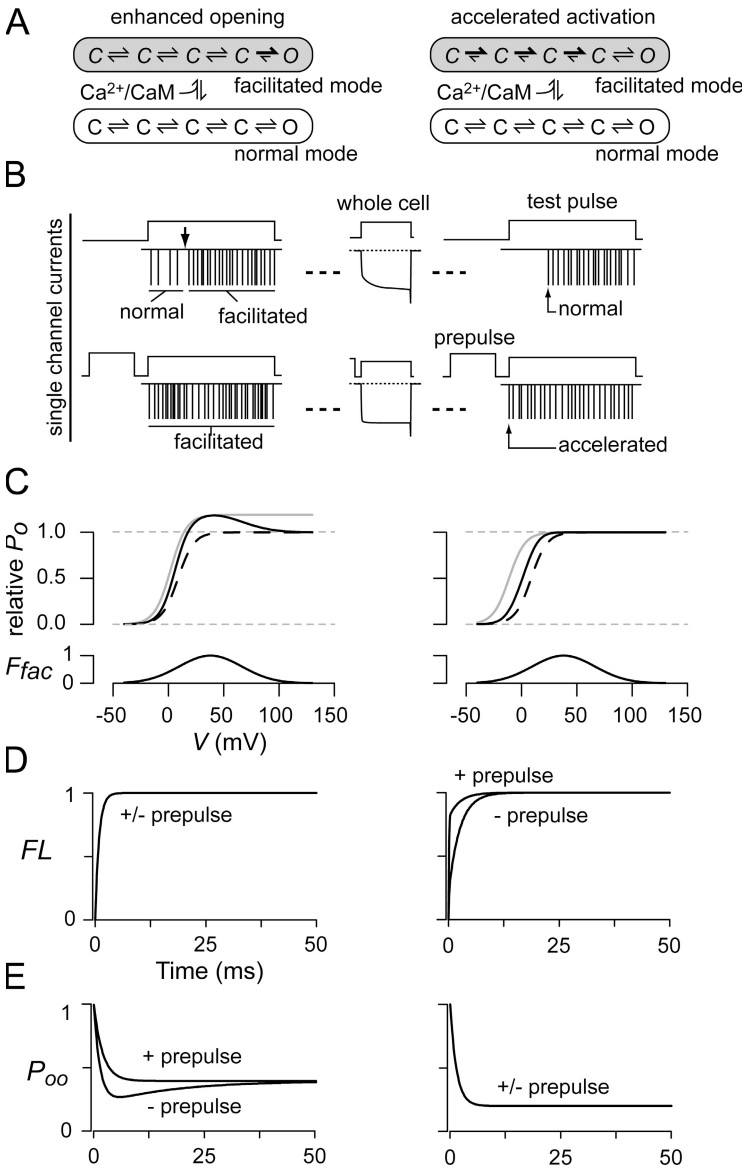

Figure 3. Potential elementary mechanisms underlying macroscopic CDF. (A) State diagram representation of mechanisms. For the enhanced-opening mechanism (left), the normal mode of gating (states within white box) features rapid activation with a lower P_o after first opening, whereas the facilitated mode (states within gray box) supports nearly identical activation with a higher P_o after first opening. Ca^{2+} binding to CaM drives the transition from normal to facilitated modes, thereby producing CDF. C represents a closed conformation, and O represents an open conformation. For the accelerated-activation mechanism (right), the normal mode exhibits a delayed time to first opening, but an appreciable P_o thereafter. The facilitated mode sports fast first opening, but the same P_o thereafter. (B) Cartoons of expected single-channel activity for the enhanced-opening (left) and accelerated-activation (right) mechanisms. Top, anticipated activity for test pulse depolarization without prepulse. Bottom, expected activity for test pulse with prepulse. Labels denote gating mode associated with indicated segments of activity; arrow marks transition between modes. Either scenario (left or right) would give rise to the well-studied macroscopic profile of CDF, schematized in the center of the panel. (C) Expected distinctions between the two mechanisms, when probed with macroscopic tail current analysis (e.g., Fig. 4). The enhanced-opening mechanism (left) predicts a hump-shaped relative P_o curve as determined from tail current measurements. This distinctive shape arises from the smaller plateau level of steady-state P_o curves for the normal (black dashed curve) versus facilitated modes of gating (gray curve), the weighted average of which produces the measured relative P_o curve (solid black). The relevant weighting factor is F_{fac}, the fraction of channels in the facilitated mode at the end of the test depolarization just before capturing tail currents. The accelerated-activation mechanism predicts a measured relative P_o curve (solid black) that lacks an overshoot hump. For short 20-ms depolarizations before tail current measurement, the corresponding P_o curves for normal (gray) and facilitated modes of gating (black dashed) are simply voltage shifted with respect to each other, such that their weighted average cannot produce an overshoot. (D and E) Expected single-channel outcomes for enhanced-opening (left) and accelerated-activation (right) mechanisms. *FL* is the probability that a first opening occurs before time *t* in the test pulse depolarization (D), whereas P_{oo} is the probability of finding a channel open with a delay *t* after a channel is known to have had a first opening (E). The enhanced-opening mechanism predicts no prepulse dependence of *FL* (D, left), but a characteristic prepulse dependence of P_{oo} (E, left). The accelerated-activation mechanism will show just the opposite profile (D and E, right) (see text for further details).

yields a relative measure of $P_o(V_{step})$. Importantly, the $P_o(V_{step})$ that we measure in this way represents a type of weighted average of the voltage-dependent activation profiles for normal and facilitated modes of gating. This experimental P_o metric thereby predicts different outcomes for enhanced opening versus accelerated activation mechanisms (Fig. 3 A).

For the enhanced opening mechanism, the steady-state P_o-V relation for the facilitated gating mode (Fig. 3 C, left, gray curve) would be larger in amplitude, and possibly leftward shifted, compared with the relation for the normal mode (black dashed curve). Because the voltage step furnishes ample time for channels to reach steady state in either gating mode of this scenario, the experimental activation curve determined from tail currents (Fig. 3 C, left, black solid curve) should reflect a true weighted average of the steady-state relations for each mode in isolation (gray and black dashed curves), where the weighting is by the fraction of channels in each mode at the end of the step depolarization. Because the fraction of facilitated channels at the end of the step (Fig. 3 C, bottom, F_{fac}) will be proportional to the Ca^{2+} influx driving CDF, and Ca^{2+} entry itself features a bell-shaped voltage dependence, it follows that F_{fac} should also demonstrate a like biphasic profile. The enhanced opening mechanism would therefore predict

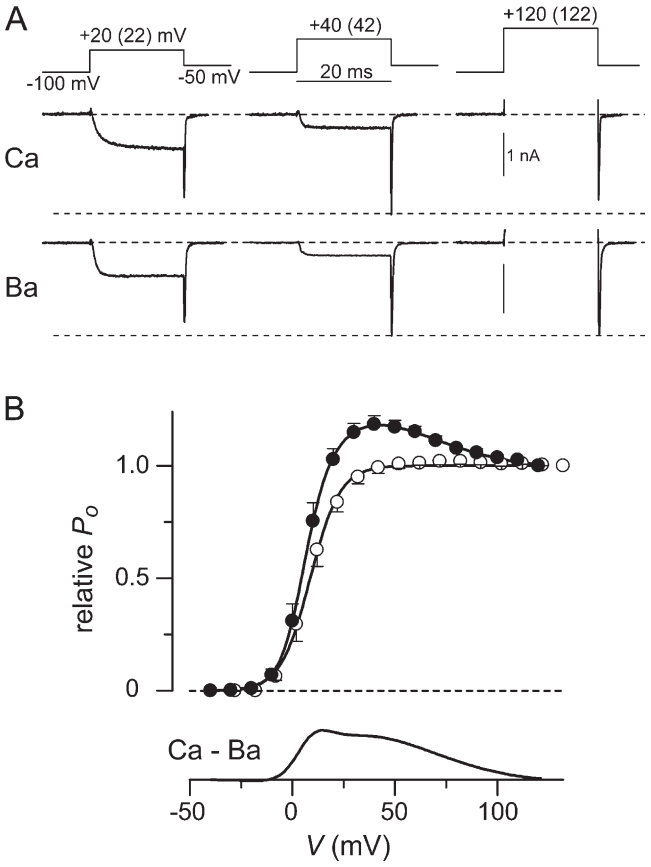

Figure 4. Macroscopic tail current activation curves favor the enhanced-opening mechanism of CDF. (A) Exemplar tail current records. Top, voltage protocol, with parenthetical values pertaining to Ba^{2+} currents shown below. Middle, Ca^{2+} tail currents. Bottom, Ba^{2+} tail currents. 5 mM Ca^{2+} or Ba^{2+} as charge carrier. Outward currents were clipped for clarity. (B) Top, mean tail current activation curves for Ba^{2+} currents (open circles, averaged from $n = 5$ cells) and Ca^{2+} currents (filled circles, averaged from $n = 5$ cells). Tail currents have been normalized by amplitudes recorded after the most extreme depolarizations shown. Ba^{2+} voltages have been shifted 12 mV in the depolarizing direction, to account for the surface charge shift between Ca^{2+} and Ba^{2+} currents. Smooth curve fits by eye. Bottom, difference of smooth fits to Ca^{2+} and Ba^{2+} data above, furnishes a rough indication of presumed F_{fac} function (Fig. 3 C).

a distinctive experimental activation curve with an "overshoot hump" (Fig. 3 C, left, solid black curve), which should be centered around voltages that maximize Ca^{2+} influx during the step.

For the accelerated-activation mechanism, both normal and facilitated modes support similar P_o-V relations at steady state, as these modes are defined by comparable P_o values after initial opening (Fig. 3 C, right, gray curve). However, though facilitated channels would activate quickly enough to reach their steady-state profile within the 20-ms test pulse, slower-to-activate channels within the normal mode of this mechanism would not achieve steady state, yielding an effective activation curve that would appear right shifted (Fig. 3 C, right, black dashed curve). Curves for the two modes would likely exhibit the same plateau level at saturating depolarization, because very strong depolarization would probably produce sufficient acceleration of normal channel activation to permit attainment of steady-state gating. Accordingly, by using the anticipated F_{fac} function (Fig. 3 C, right, bottom), the weighted average of these two P_o-V relations (Fig. 3 C, right, gray and black-dashed curves) predicts an experimental activation curve that lacks a tell-tale hump (Fig. 3 C, right, black solid curve).

Fig. 4 summarizes the results for the actual tail current experiments. With Ca^{2+} as charge carrier, tail current amplitudes are indeed maximized by an intermediate step depolarization to ~40 mV (Fig. 4 A, middle). With either more hyperpolarized (20 mV) or depolarized (120 mV) voltage steps, tail currents are comparatively smaller. By contrast, corresponding Ba^{2+} tail currents increase monotonically with strengthened depolarization (Fig. 4 A, bottom), as expected for channels trapped within a normal gating mode. Activation curves, averaged from $n = 5$ cells after normalizing to responses for the 120-mV depolarization, confirm a clear overshoot in the Ca^{2+} activation curve (Fig. 4 B, solid circles), which is absent with Ba^{2+} (open circles). Subtracting these activation curves reveals a bell-shaped curve (Fig. 4 B, bottom), analogous to that expected for F_{fac} (Fig. 3 C, bottom). These results suggest that an enhanced opening mechanism is at least partly responsible for CDF. However, this type of data does not exclude the additional presence of accelerated activation, nor is the interpretation favoring enhanced opening entirely independent of assumptions regarding the behavior of P_o-V relations for the different gating modes.

In Depth Single-Channel Analysis of CDF

Rigorous statistical analysis of single-channel activity promises a more definitive dissection of CDF mechanisms. Direct visual inspection of unitary currents provides an initial indication of the underlying CDF mechanism. Indeed, exemplar records (Fig. 2 A) hint at a period of sparser opening near the onset of voltage steps without a prepulse (Fig. 2 A, gray bar period), which is nearly absent following a prepulse. These records also fail to suggest marked prepulse-dependent differences in the time to first opening (first latencies). These visual trends thereby give the impression of an enhanced opening mechanism. More rigorously, the single-channel data permit accumulation of histograms describing first latency probability (FL) and conditional open probability (P_{oo}) functions, as theoretically portrayed in Fig. 3 (D and E). These two metrics are ideally poised to distinguish among CDF mechanisms, as follows. $FL(t)$ quantifies the probability that the first channel opening occurs before a time t within the test pulse, and fully incorporates the kinetics of initial channel

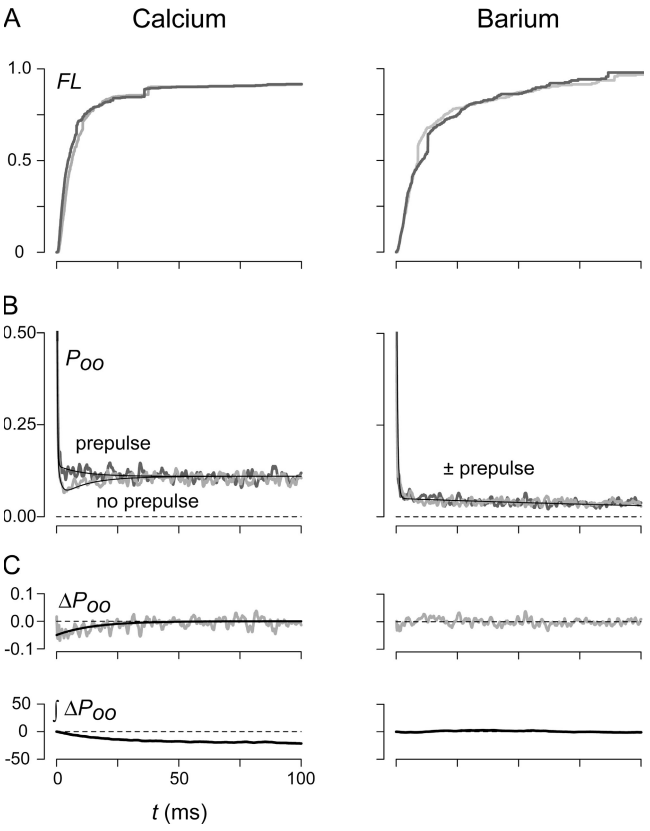

Figure 5. In depth single-channel analysis supports a nearly exclusive enhanced-opening mechanism. For all panels, the left column pertains to mean statistical profiles for unitary Ca^{2+} currents through $Ca_V2.1$ channels (EF_a splice variant), whereas the right column concerns mean statistics for unitary Ba^{2+} currents through the same type of channels. (A) *FL* functions measured with (black curve) and without (gray curve) a preceding prepulse. There is no appreciable prepulse dependence. Ca^{2+} curves averaged from $n = 5$ patches; Ba^{2+} curves from a different $n = 4$ patches. (B) P_{oo} functions measured with (black curve) and without (gray curve) a prepulse. Smooth curves fit by eye. The Ca^{2+} relation obtained without a prepulse exhibits the characteristic "dip" expected for an enhanced opening mechanism. Ca^{2+} data averaged from $n = 5$ patches. Ba^{2+} data averaged from a different $n = 5$ patches. (C) Top, difference of mean P_{oo} relations in B (no prepulse P_{oo}–prepulse P_{oo}). Bottom, time integral of difference relations above (ms units, shown at 20× amplification). Top left, difference relation for Ca^{2+} currents fit by eye with single exponential function with a time constant of 20 ms.

activation (Aldrich and Stevens, 1983). $P_{oo}(t)$, on the other hand, is the conditional open probability that a channel will be found open with a delay t after a first opening; this measure thereby specifies aggregate channel gating after the initial activation event. Together, these two functions constrain the overall gating characteristics of a channel (Sigworth, 1981; Aldrich and Stevens, 1983; Imredy and Yue, 1994; Patil et al., 1996; Colecraft et al., 2001) and project very different outcomes for the contrasting CDF mechanisms. For the enhanced opening scheme, *FL* curves derived from test pulses with or without a prepulse should be nearly identical (Fig. 3 D, left), because initial gating is not appreciably different in normal versus facilitated gating modes. However, the accelerated activation mechanism predicts faster rising *FL* curves following a prepulse, since facilitated channels would first activate faster in this scenario (Fig. 3 D, right). With the P_{oo} function, the situation is reversed. The enhanced opening hypothesis posits that, during isolated test pulses, the conditional P_o following first opening would initially feature a small value ($P_o \sim 0.04$), which would then transition to a larger level ($P_o \sim 0.09$). This effect should be visible as a dip in the P_{oo} curve before reaching a plateau at longer t (Fig. 3 E, left). For test pulses that follow a prepulse, the dip should be absent, as channels open directly to the $P_o \sim 0.09$ level. Conversely, in the accelerated activation hypothesis, no difference exists in the conditional P_o subsequent to first opening, so P_{oo} curves from test pulses should be almost identical without regard to a preceding prepulse (Fig. 3 E, right).

Turning to our data, in depth single-channel analysis furnishes definitive evidence favoring the predominance of an enhanced opening mechanism for CDF (Fig. 5). First, *FL* distributions for Ca^{2+} appear essentially identical without regard to the presence of prepulse depolarization (Fig. 5 A, left, average from $n = 5$ patches), contradicting an accelerated activation model. In Ba^{2+}, *FL* curves also appear superimposed (Fig. 5 A, right, average from $n = 4$ patches). Second, P_{oo} curves with Ca^{2+} do indeed show prepulse-dependent changes characteristic of the enhanced opening mechanism. Without a prepulse, the P_{oo} curve dips to a low point (~ 0.04) before transitioning to a higher plateau with $P_{oo} \sim 0.09$ (Fig. 5 B, left, gray curve average of $n = 5$ patches). With a prepulse, the P_{oo} rapidly achieves the higher level without evidence of a dip (black curve average of $n = 5$ patches). These prepulse-dependent differences are confirmed by calculating the difference between P_{oo} curves (Fig. 5 C, top left), which reveals a roughly single-exponential decay, with time constant ~ 20 ms. By integrating this difference, we emphasize further the significance of the difference curve, as the integrated relation flattens out at a distinctly negative value (Fig. 5 C, bottom left). Third, these prepulse-dependent differences in P_{oo} clearly reflect CDF, because of their complete absence in the case of Ba^{2+} activity (Fig. 5 B, right). Here, regardless of prepulse, the P_{oo} functions decay immediately to the same lower level of ~ 0.04, without indication of a dip. In all, the nearly exact correspondence of these actual *FL* and P_{oo} profiles to those predicted for the enhanced opening scheme (Figs. 3, D and E, left) furnishes direct support for this mechanism of CDF.

Trapping of EF_b Splice Variants of $Ca_V2.1$ Channels within a Normal Gating Mode

Splice variation of Ca_V Ca^{2+} channels permits impressive functional customization for specialized biological

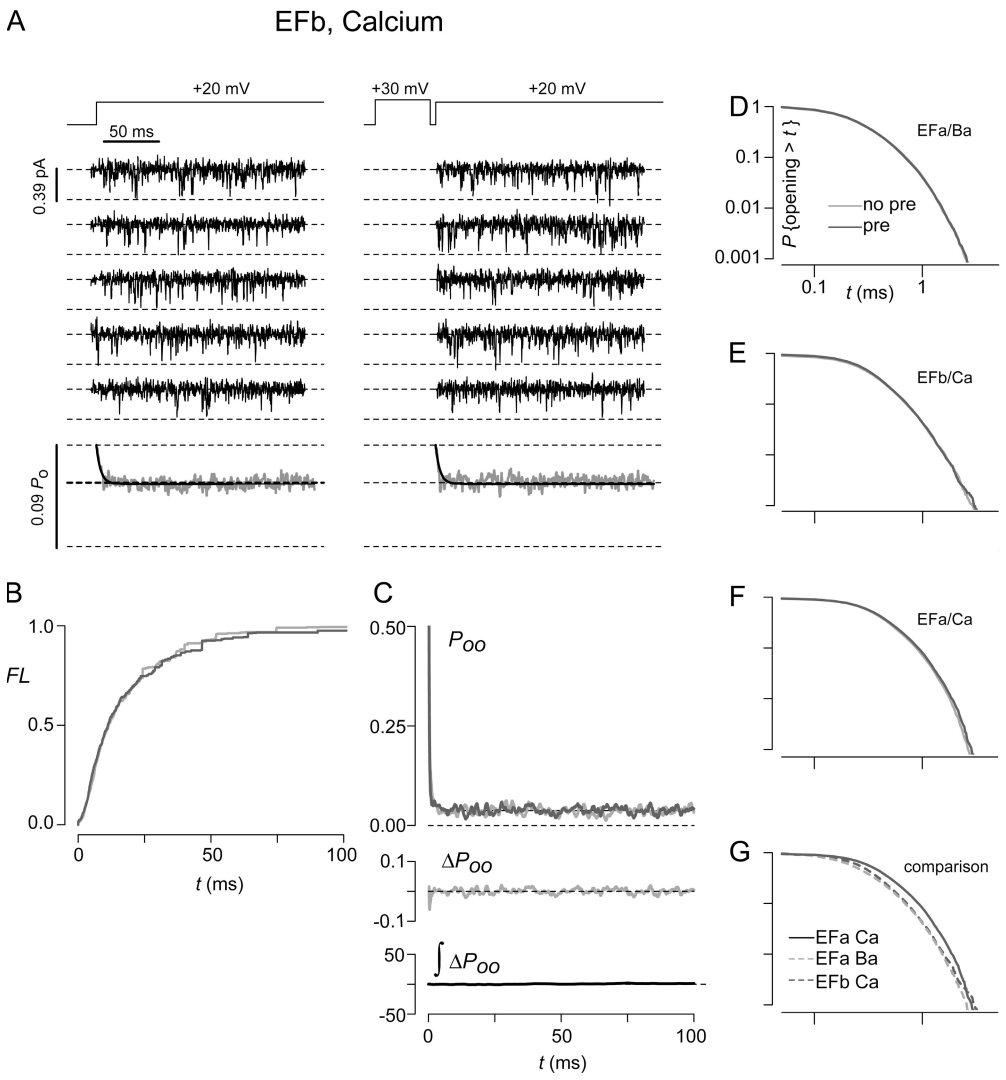

Figure 6. Unitary Ca^{2+} currents through the EF_b splice variant of P/Q-type channels (A–C). (A) Exemplar unitary Ca^{2+} current records and ensemble averages, using an identical protocol and display format as in Fig. 2 A. Exemplar records are from a patch with a single channel. Ensemble averages are derived from $n = 5$ patches. (B and C) In depth single-channel analysis of these EF_b splice variant channels, indicating channel trapping within the normal mode of gating. Format identical to that in Fig. 5 (A–C). All data averaged from $n = 5$ patches. (D and E) Open-time histogram analysis for various experimental configurations, shown as $P\{\text{opening} > t\}$ versus t on a log–log plot. Black curves pertain to data obtained after a prepulse (pre), whereas gray curves concern data recorded without a prepulse (no pre). (D) Open-time histograms for unitary Ba^{2+} currents through EF_a channels, averaged from $n = 5$ patches. $t_{1/2} = 0.295$ ms (no prepulse); $t_{1/2} = 0.270$ ms (prepulse). (E) Open-time histograms for unitary Ca^{2+} currents through EF_b channels, averaged from $n = 4$. $t_{1/2} = 0.249$ ms (no prepulse); $t_{1/2} = 0.252$ ms (prepulse). (F) Open-time histograms for unitary Ca^{2+} currents through EF_a channels, averaged from $n = 5$ patches. $t_{1/2} = 0.410$ ms (no prepulse); $t_{1/2} = 0.385$ ms (prepulse). (G) Superposition of open-time histograms (with prepulse) reproduced from D–F. Unitary Ca^{2+} currents through EF_a channels support the longest open times.

contexts (Lipscombe et al., 2002; Lipscombe and Castiglioni, 2003). In this regard, another worthy application of single-channel analysis concerns the behavior of a fascinating EF_b splice variant of $Ca_V2.1$, wherein alternative splicing at a single exon ablates CDF of these channels (Chaudhuri et al., 2004; Chaudhuri et al., 2005). All experiments described thus far in this study have used the EF_a splice variant of $Ca_V2.1$, which is permissive for CDF. An important question is whether EF_b channels are trapped within the normal versus facilitated mode of gating. This question remains open, as sequestration within either mode would explain the observed insensitivity of macroscopic Ca^{2+} currents to prepulse depolarization.

Fig. 6 summarizes single-channel data, which definitively indicate that EF_b channels are restricted to the normal mode of gating, as portrayed in the enhanced opening scheme of Fig. 3 A (left). Regardless of prepulse, unitary Ca^{2+} currents from this splice variant exhibit a sparser gating pattern (Fig. 6 A, middle), and the ensemble averages invariably demonstrate a lower overall P_o of ~0.04 (Fig. 6 A, bottom, averaged from $n = 5$ patches). Moreover, both FL and P_{oo} functions exhibit strict prepulse insensitivity (Fig. 6, B and C), and the P_{oo} relation decays directly to a plateau value of ~0.04. These two relations quantitatively recapitulate the fingerprint of isolated normal mode gating, as gauged by the corresponding metrics for unitary Ba^{2+} currents of EF_a channels (Fig. 2 B and Fig. 5).

This entrapment of EF_b channels (and of EF_a channels with Ba^{2+}) motivates a final dissection of CDF mechanisms using more traditional methods. More precisely, captivity within a single gating mode simplifies the application of classical open-duration histogram

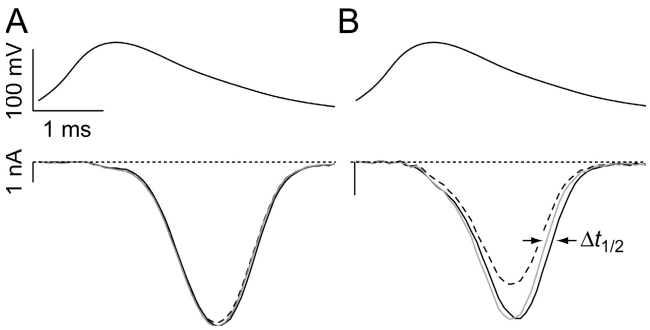

Figure 7. Resolving dual dimensions of APW-induced current augmentation, as predicted by the enhanced-opening mechanism of CDF. (A) Alignment of first (dashed black curve) and maximal Ba^{2+} current responses (solid black curve) from APW train experiment in Fig. 1 A. Upward scaling of the first response, to match the amplitude of the maximal response, yields a scaled waveform (gray curve) that superimposes the maximal response (black solid curve). (B) Alignment of first (dashed black curve) and maximal Ca^{2+} current responses (solid black curve) from APW train experiment in Fig. 1 A. Upward scaling of the first response yields a scaled waveform (gray curve) that decays earlier than the maximal response (black solid curve). Hence, CDF yields Ca^{2+} responses that are both larger and longer lasting, as predicted by the enhanced opening mechanism. The accelerated-activation mechanism would predict only an increase in amplitude, without change in longevity.

analysis (Colquhoun and Hawkes, 1982), for which straightforward implementation requires a minimum of complex mode switching. Because egress from the open state is potentially slower in the facilitated versus normal gating mode of the enhanced opening scheme, open durations might be (a) identically short for channels imprisoned within the normal mode, and (b) prolonged for channels strongly enriched for facilitated openings. Alternatively, the accelerated activation model would predict similar open durations for both instances, as gating is presumed similar after first opening. Support for the first prediction comes from the indistinguishably brief open durations for Ba^{2+} currents through EF_a channels (Fig. 6 D) and Ca^{2+} currents through EF_b channels (Fig. 6 E). As expected, neither of these configurations exhibit detectable prepulse dependence, because of restriction to the normal gating mode. As for the second prediction, the mode switching of unitary Ca^{2+} currents through EF_a channels would seemingly complicate interpretation of open times as cleanly representative of either normal or facilitated configurations in seclusion. Further consideration would, however, suggest that although channels may spend a visible span of time within the normal gating mode (Fig. 2 A, gray bar period, no prepulse case), the numerically few openings that occur within this sparse pattern of activity will be far outweighed by the vast number of openings within the presumed facilitated context. Hence, even without prepulse, the open duration histogram should very nearly reflect properties of the facilitated gating mode viewed in isolation. Consistent with this view, open durations for Ca^{2+} currents through EF_a channels are essentially independent of prepulse depolarization, and elongated relative to the other configurations (Fig. 6 F). Superposition of open time histograms for the various contexts explicitly emphasizes these findings (Fig. 6 G). For clarity, only data following prepulse depolarization are shown in the latter overlay. Overall, this open duration analysis supports an enhanced opening mechanism for CDF, along with confinement of channels to the normal gating mode (EF_a carrying Ba^{2+} currents, or EF_b channels).

Physiological Implications of Enhanced Opening versus Accelerated Activation Mechanisms

Having established the enhanced opening mechanism, we explore a correlative physiological implication of CDF, using our new mechanistic insights to reexamine the macroscopic Ca^{2+} currents evoked by action-potential waveform (APW) trains (Fig. 1 A). The spike-to-spike increases of Ca^{2+} current amplitude reflects a net increase in the product of two multiplicative factors: the probability of observing a channel open at least once during a particular stimulus (P_{gate}), and the conditional P_o given that at least one opening does occur ($P_{o|gate}$). The enhanced-opening mechanism predicts that repetitive spike activation would leave P_{gate} largely unchanged, because *FL* is little changed in this kinetic framework. Instead, the increased current would mainly reflect progressive augmentation and prolongation of $P_{o|gate}$, as driven by conversion of channels to a facilitated mode with higher characteristic P_o, but similar activation kinetics. Hence, macroscopic current responses should not only become larger, but longer lasting. By contrast, an accelerated-activation mechanism would predict only a boost in P_{gate}, reflective of changes in *FL*. Because gating after first opening is unchanged with facilitation in this context, $P_{o|gate}$ would remain largely unchanged. Accordingly, macroscopic currents should increase in amplitude alone, without alteration in waveform shape. We test for these predictions by normalizing the peak amplitudes of currents evoked by the first stimulus to those seen for the largest subsequent response during an APW train. With Ba^{2+} as charge carrier, there is an insignificant increase in current during trains (Fig. 1 A, bottom; 103 ± 1% increase, $n = 3$ cells, n.s.). Moreover, first and maximal Ba^{2+} responses show the identical waveform shape after normalization (Fig. 7 A, bottom). For quantification of normalized waveform duration, we measure the difference in time at which waveforms relax to half-maximal amplitude ($\Delta t_{1/2} = 13 \pm 13$ μs, $n = 3$ cells, n.s.). By contrast, Ca^{2+} responses for EF_a channels not only showed significant increases in amplitude (Fig. 1 A, 122 ± 5%, $n = 3$ cells, $P < 0.05$ compared with Ba^{2+}), but also substantial waveform prolongation (Fig. 7 B, $\Delta t_{1/2} = 120 \pm 23$ μs, $n = 3$ cells, $P < 0.05$

compared with Ba^{2+}). This bidimensional augmentation of spike responses (amplitude and duration), as suggested by the enhanced opening mechanism, may entail significant biological consequences, given the power-law relationship between presynaptic Ca^{2+} influx and neurotransmitter release (Dodge and Rahamimoff, 1967), as well as the exquisite spatio-temporal coupling of Ca^{2+} sources to vesicle release (Zucker and Regehr, 2002). For example, prolongation of spike-evoked Ca^{2+} responses by 100–200 μs, even without appreciable change in peak amplitude, can enhance post-synaptic EPSCs by two to threefold (Sabatini and Regehr, 1997). More broadly, spike-dependent changes in Ca^{2+} currents have also been observed in the context of dynamic G-protein inhibition of Ca_V2 channels (Brody et al., 1997; Park and Dunlap, 1998). The activity-dependent relief from inhibition for certain $Ca_V2.2$ channels is akin to an enhanced opening mechanism (Colecraft et al., 2001) and supports spike-dependent enhancement of current amplitude and duration. By contrast, the analogous reversal of G-protein inhibition in $Ca_V2.1$ channels involves an accelerated activation scheme (Colecraft et al., 2001), and spike-dependent augmentation of current transpires by changes in amplitude alone.

DISCUSSION

This paper reports on the first extensive single-channel analysis of $Ca_V2.1$ channels permeated with the physiological charge carrier Ca^{2+}. These recordings resolve fundamental mechanistic unknowns regarding the CaM-mediated Ca^{2+} feedback of these channels. First, we provide direct evidence that CDF (triggered by the C-lobe of CaM) responds to a local Ca^{2+} signal, whereas CDI (triggered by the N-lobe of CaM) requires a global Ca^{2+} signal. This demonstration substantiates key features of a general rule of spatial Ca^{2+} preference concerning the C- versus N-lobe of CaM, as seen for CaM regulation across the family of Ca_V1-2 channels (Liang et al., 2003). Second, independent lines of evidence from customized whole-cell and single-channel experiments demonstrate that CDF results from a genuine enhancement of channel opening probability over a basal level, rather than derepression of channel P_o or acceleration of activation kinetics. Splice variation at an EF-hand locus of $Ca_V2.1$ channels can restrict conformations to a normal gating mode, which supports the basal level of activity. Third, the enhanced-opening mechanism may support increases in both the amplitude and duration of Ca^{2+} currents evoked during repetitive physiological stimuli. This section contextualizes these new data within the body of prior single-channel experiments, broadens the neurobiological implications of the spatial Ca^{2+} selectivity of CaM regulatory mechanisms revealed here, and explores the generality of the enhanced opening mechanism of CDF.

Relation to Prior Single-Channel Studies of $Ca_V2.1$

The requirement of Ca^{2+} to activate CaM/channel regulation necessitates the use of Ca^{2+} as charge carrier in this study. This constraint entails 2–3× smaller unitary amplitudes (i) for Ca^{2+} versus the previously employed Ba^{2+} currents (Tottene et al., 2002). Accordingly, the present single-channel experiments feature test potentials (~20 mV) that are moderately less positive than those achieved (~45 mV) in a subset of prior experiments with Ba^{2+} (Colecraft et al., 2001; Fellin et al., 2004), because the diminished driving force at more positive potentials would render unitary Ca^{2+} currents too small for reliable resolution. Nonetheless, the channel properties detailed here are consistent with those of previous reports, where overlapping voltage ranges are considered. Our Ba^{2+} current amplitudes are consistent with those reported previously, and channel P_o was in the range of prior observations (Dove et al., 1998; Hans et al., 1999; Colecraft et al., 2001; Tottene et al., 2002; Fellin et al., 2004; Luvisetto et al., 2004; Tottene et al., 2005). In particular, the overall P_o of ~0.04 with Ba^{2+} in this study matches well with that estimated for a test potential of 20 mV in our prior single-channel report (Colecraft et al., 2001). Moreover, two other recent analyses of $Ca_V2.1$ single-channel properties also merit specific comparison. In these reports, several modal gating behaviors were observed with Ba^{2+}, including a highly active (fast) or less active (slow) gating mode (Fellin et al., 2004; Luvisetto et al., 2004). Our channel activity appears to correspond best to the slow mode of gating, as seen from our overall P_o of ~0.04 with Ba^{2+}. Two reasons may account for the dearth of detectable fast gating in our records. First, due to the convergence of P_o values for fast and slow gating modes at more hyperpolarized potentials (Luvisetto et al., 2004), such as employed in the present experiments, both gating patterns may have effectively coalesced into a single lower P_o mode. Second, the use of a different auxiliary subunit (β_{2a}) in the present experiments (to minimize VDI and enhance resolution of CDI/CDF) could also rationalize the apparent difference in modal gating behavior, as different β subunits are known to confer customized gating profiles (Luvisetto et al., 2004). Fitting with this explanation, in our prior $Ca_V2.1$ single-channel experiments with β_{2a}, we did not resolve fast and slow gating patterns in Ba^{2+} currents evoked with stronger depolarizations, and instead observed a uniform pattern of gating (Colecraft et al., 2001). Nonetheless, the single-channel CDF mechanisms that we observe will likely generalize, at least in coarse outline, to channel configurations with other auxiliary subunits, because macroscopic CDF is a robust phenomenon seen with different β subunits over a wide range of depolarizations (Chaudhuri et al., 2005). Future experiments using different β subunits are required to test explicitly for such generalization.

An important caveat relating to the majority of single-channel data in the literature concerns the use of ~100 mM charge carrier to facilitate resolution of unitary currents. This limitation also pertains to the present study and merits some caution in quantitative extrapolation to the physiological context where ~2 mM Ca^{2+} is the charge carrier. On the other hand, whole-cell records using near physiological Ca^{2+} do exhibit similar phenomena to those produced by single-channel activity (compare Fig. 1 B and Fig. 2). This latter concordance argues that qualitative extrapolations between the two regimes are warranted.

Neurobiological Implications of the Spatial Ca^{2+} Selectivity of CaM-mediated Feedback

Over the past several years, whole-cell experiments probing CaM/Ca^{2+} channel regulation have hinted at the existence of an intriguing design principle for the spatial Ca^{2+} selectivity of the lobes of CaM (Liang et al., 2003). Across the Ca_V1-2 channel family, different forms of CaM/channel regulation can be initiated by Ca^{2+} binding to one lobe of CaM or the other (Peterson et al., 1999; DeMaria et al., 2001; Lee et al., 2003; Liang et al., 2003). In the extreme, two different regulatory processes can be observed within a single channel type (e.g., CDI and CDF of $Ca_V2.1$; or slow and fast CDI in $Ca_V1.3$), with each process selectively triggered by Ca^{2+} binding to a different lobe of CaM (DeMaria et al., 2001; Yang et al., 2006). Remarkably, whenever Ca^{2+} binding to the C-terminal lobe of CaM triggers regulation, this regulation is insensitive to strong Ca^{2+} buffering, even by several millimolar concentrations of the rapid chelator BAPTA (Zuhlke and Reuter, 1998; DeMaria et al., 2001; Soong et al., 2002; Chaudhuri et al., 2004, 2005). Such buffering would zero Ca^{2+} everywhere except within the very local nanodomain of Ca^{2+} channels (Augustine et al., 2003). Moreover, the strength of such regulation is largely independent of current amplitude (Peterson et al., 1999; Soong et al., 2002; Chaudhuri et al., 2004, 2005; Yang et al., 2006), which serves as an indicator of the global Ca^{2+} signal. The indirect inference from these experiments is that the C-terminal lobe of CaM responds preferentially to local Ca^{2+} signals. The only known exception to this trend is the CDF (mediated by the C-terminal lobe) for a particular splice variant of P/Q-type channels (EF_b with exon 47 present), which exhibits a partial global Ca^{2+} preference (Chaudhuri et al., 2004). By overall contrast, whenever Ca^{2+} binding to the N-terminal lobe of CaM initiates channel modulation, this modulation is strongly sensitive to Ca^{2+} buffering (Lee et al., 2000; DeMaria et al., 2001; Soong et al., 2002; Liang et al., 2003), and the strength of this modulation is clearly correlated with whole-cell current amplitudes (Soong et al., 2002; Yang et al., 2006). Hence, it would appear that the N-terminal lobe of CaM is selective for global Ca^{2+} signals, even though the relevant CaM molecule appears constitutively bound to channels within the nanodomain. That this pattern holds true across multiple Ca_V1-2 channels suggests that this pattern of spatial Ca^{2+} selectivity reflects a general principle (Liang et al., 2003).

The single-channel experiments in this study (Fig. 2 A) furnish the most direct evidence to date for this pattern of spatial Ca^{2+} preference. By definition, a single channel can only produce a local Ca^{2+} signal, but not a global Ca^{2+} signal. Hence, the preservation of CDF (driven by the C-lobe of CaM) and absence of CDI (induced by the N-lobe) within single $Ca_V2.1$ channels directly demonstrates the distinctive spatial Ca^{2+} preferences of the lobes of CaM. It might be questioned whether the lack of single-channel CDI is trivially produced by depolarizing to a potential (+20 mV) that is nonpermissive for CDI, considering that the CDI of macroscopic currents is only apparent over a certain voltage range (Chaudhuri et al., 2004). However, macroscopic current data also indicate that the permissive voltages for CDF and CDI are coincident (Chaudhuri et al., 2004). Hence, the presence of strong CDF in single-channel patches confirms that the lack of CDI is not trivially produced by an inappropriate test potential, and that the mechanistic deductions concerning spatial Ca^{2+} selectivity hold true. An important contrasting control for the lack of CDI in single $Ca_V2.1$ channels is the clear CDI of $Ca_V1.2$ channels observed at the single-channel level (Yue et al., 1990; Imredy and Yue, 1994). Here, the CDI is triggered by Ca^{2+} binding primarily to the C-terminal lobe of CaM, and would be expected to be responsive to local Ca^{2+} signals (Peterson et al., 1999). Of further importance, the intracellular Ca^{2+} buffering status in these single-channel experiments is completely unperturbed from the native configuration, as no intracellular dialysis occurs in the on-cell patch-clamp configuration that we used (Hamill et al., 1981). Hence, the proposed lobe-specific pattern of spatial Ca^{2+} selectivities is relevant to native cells, not only those in which whole-cell dialysis of the intracellular milieu may have inadvertently accentuated such a pattern. Experiments that probe unitary Ca^{2+} currents through other Ca_V1-2 channels can further extend the generality of CaM lobe-specific selectivities for spatial Ca^{2+} signals.

Given the strong evidence for lobe-specific spatial Ca^{2+} preference in $Ca_V2.1$ channels, it is worth considering obvious neurobiological implications of this selectivity (Evans and Zamponi, 2006). In particular, as $Ca_V2.1$ channels comprise the dominant Ca^{2+} trigger of synaptic transmission within the central nervous system (Wheeler et al., 1994; Dunlap et al., 1995; Wheeler and Tsien, 1999), their dynamic regulation by Ca^{2+} may impact neuronal information transfer via short-term synaptic plasticity (Tsodyks and Markram, 1997; Tsodyks

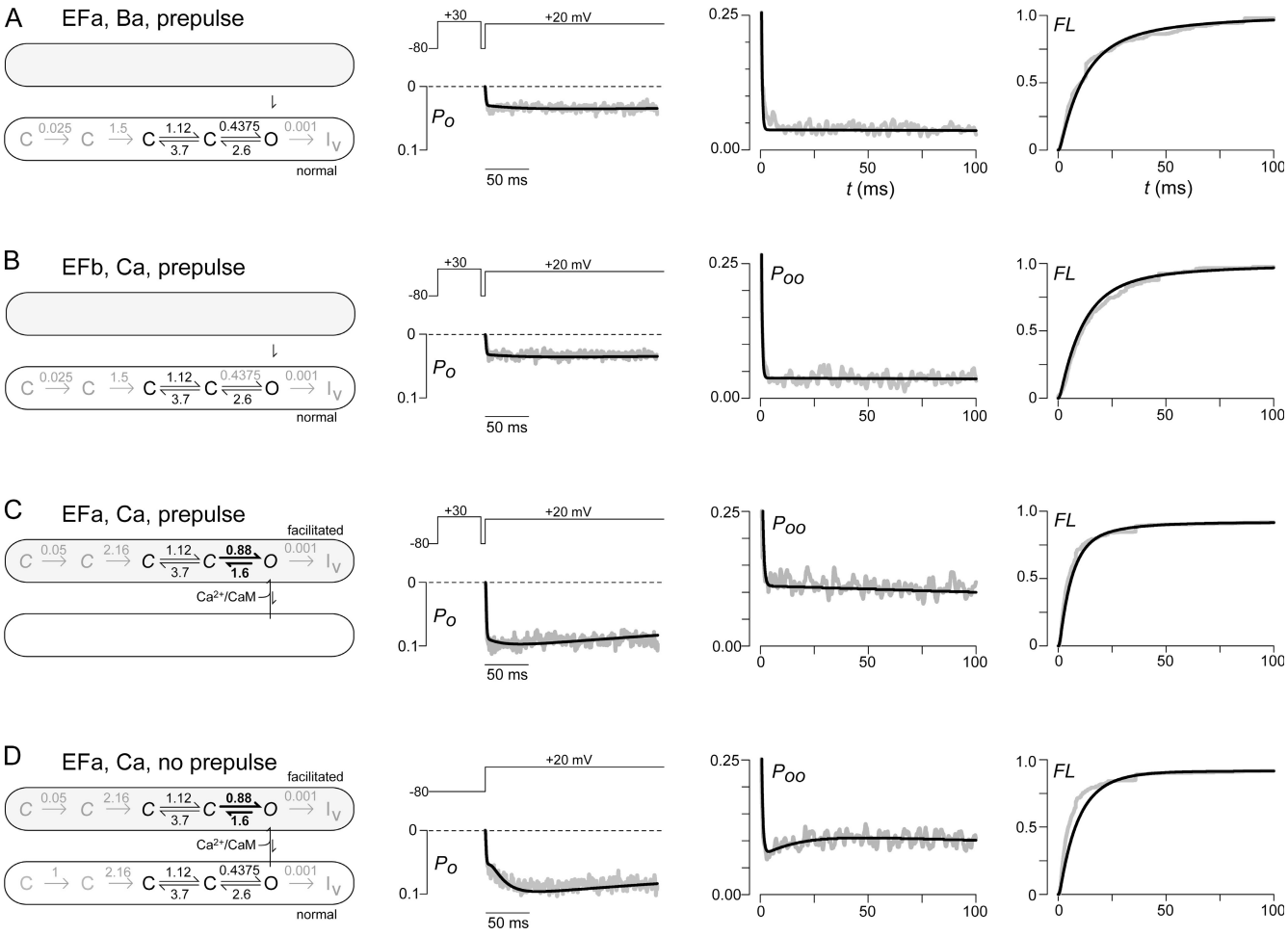

Figure 8. Explicit kinetic simulations of the enhanced-opening mechanism furnish a global quantitative explanation for multiple single-channel datasets. (A) Simulations of unitary Ba^{2+} activity through channels bearing the EF_a splice variant. Far left, kinetic layout and rate-constant parameters for transitions within the normal mode of gating at a step potential of +20 mV (white rectangle). Numerical values are in units of ms^{-1}. Parameters and states shown in black are best determined, being doubly constrained by P_o and P_{oo} functions. Those displayed in gray impart subtle improvements to the overall fit, but are less well constrained. Mean experimental P_o (center left), P_{oo} (center right), and *FL* (far right) are reproduced from earlier data figures as gray traces (prepulse data only). The initial conditions of the P_o and *FL* simulations featured 20% of available channels in the leftmost closed state, and 80% of available channels in the immediately adjacent closed state. Superimposed upon these plots are the kinetic simulations of the enhanced-opening mechanism (black curves), with parameters on the far left. (B) Simulations of unitary Ca^{2+} activity through EF_b channels, using identical parameters as in A, except that the initial conditions of P_o and *FL* simulations featured 15% of available channels in the leftmost closed state, and 85% of available channels in the immediately adjacent closed state. Format as in A. (C) Simulations of unitary Ca^{2+} activity through EF_a channels, after a prepulse. Format as in A, except that these data help constrain the facilitated mode parameters (gray rectangle) in relative isolation. The main difference of the facilitated mode, as compared with the normal mode (A and B), concerns only the transitions between the final closed and open states (shown in bold). Subtle differences in the exit transitions from the two leftmost closed states afford modest improvements of the fit to *FL* data, while voltage inactivation is left unchanged. The initial conditions of P_o and *FL* simulations featured 15% of available channels in the leftmost closed state of the facilitated mode, and 85% of available channels in the immediately adjacent closed state. (D) Simulations of unitary Ca^{2+} activity through EF_a channels, without a prepulse. Format as in A. The facilitated mode parameters are maintained exactly as in C. The normal mode parameters are identical to those used above (A and B), except for minor differences in the exit rates for the two leftmost closed states. The latter differences yield small improvements to the fit of *FL*. For P_o, P_{oo}, and *FL* simulations, the initial fraction of available channels in the facilitated mode was 35%, with 65% in the normal mode. The initial fraction of channels in the facilitated mode probably has to do with the comparatively short 6-s repetition interval used in single-channel recordings, producing some cumulative CDF. The recovery time course from CDF is ~0.5 s (DeMaria et al., 2001). Additionally, for P_o and *FL* simulations, the initial configuration was for 15% of channels in either mode to reside in the leftmost closed state, and for the remaining 85% of channels in either mode to reside in the immediately adjacent closed state. The transition from normal to facilitated modes occurs via a simple cooperative transition, as detailed in the Materials and methods.

et al., 1998; Zucker and Regehr, 2002; Abbott and Regehr, 2004). Our new insight concerning the spatial Ca^{2+} selectivity of different forms of $Ca_V2.1$ regulation suggests a strategy whereby variable blends of CDF and CDI could be produced at different types of synapses. At one extreme, the calyx of Held harbors the only synapse wherein native $Ca_V2.1$ CDF and CDI have been firmly established (Borst and Sakmann, 1998; Cuttle et al., 1998; Xu and Wu, 2005). This synapse is atypically large, with more numerous presynaptic channels and looser coupling between channels and release sites than typical for the majority of synapses (Borst and Sakmann, 1999). In this setting, one could imagine the strong presence of both local and global Ca^{2+} signals, permitting both CDF and CDI to be manifest. By contrast, for more typical synapses with few channels per release site and tighter channel-site coupling (Zucker and Regehr, 2002), only local Ca^{2+} signals would be strongly preserved, whereas global signals might be substantially diminished. The prediction here would be for strong CDF with weakened CDI, thereby favoring a facilitative synaptic profile that biases toward a high-pass or differentiating manner of synaptic transmission (Tsodyks and Markram, 1997).

Generalization of the Enhanced Opening Mechanism of CDF

Thus far, the enhanced opening mechanism accords well with all of the qualitative distinctives of this mechanism (Fig. 3). To explore the quantitative sufficiency of this gating paradigm, we here explicitly undertake kinetic simulations of the major single-channel experimental results. First, we consider averaged experimental results for P_o, P_{oo}, and *FL* for unitary Ba^{2+} currents through EF_a channels (Fig. 8 A, gray curves); these should furnish good constraints on the normal gating mode. Since experimental profiles are independent of prepulse depolarization, we have selected data from the prepulse context alone, for simplicity. The solid black curves (Fig. 8 A) show the results of simulations with the parameters displayed on the far left. The parameters shown in black are the major parameters representing this pattern of gating, being strongly constrained by both P_o and P_{oo} data. Gray parameters for deep closed states (on the left end of the normal gating mode) are included to fit nuances of the *FL* profile, and the gray parameter on the extreme right represents very slow VDI, the inclusion of which subtly improved P_o and P_{oo} fits at large *t*. Second, it is impressive that these same normal gating mode parameters (from Fig. 8 A) produce a very reasonable simulation of the averaged data for unitary Ca^{2+} currents through EF_b channels (Fig. 8 B). As for the first case, only data from the prepulse context are shown, since data are prepulse independent. The notion of entrapment within the same gating mode of EF_b channels (using Ca^{2+}), and of EF_a channels (using Ba^{2+}), finds strong support from this sufficiency of the same normal mode parameters to simulate both experimental profiles. Third, the experimental data for unitary Ca^{2+} currents through EF_a channels, as present after prepulse depolarization, should provide suitable constraints for the facilitated gating mode viewed in isolation (Fig. 8 C, gray traces). Parameters shown at the left support very reasonable fits to the data (black curves). Interestingly, the key parameter changes within the facilitated mode are mainly restricted to acceleration of the final C→O transition and slowing of the initial O→C transition. This suggests that facilitation mainly involves alterations to both opening and closing transitions very close to the ultimate open conformation. Finally, without change to the previously established parameters for normal and facilitated gating modes, we simulate the experimental profile for unitary Ca^{2+} currents through EF_a channels (Fig. 8 D). The only adjustable parameters concern transitions from normal to facilitated modes of gating. The reasonable agreement of simulations and data strongly supports the quantitative sufficiency of the enhanced opening mechanism.

Regarding a broader mechanistic perspective, we mention that the enhanced opening mechanism for $Ca_V2.1$ CDF (Fig. 8) is strikingly reminiscent of the modal switching mechanism that explains CDI of $Ca_V1.2$ channels (Imredy and Yue, 1994). The only difference is that Ca^{2+} drives transition from lower to higher P_o modes in the CDF mechanism, whereas Ca^{2+} does the inverse for the CDI scheme. Kinetic similarities extend to the manner of gating differences between modes, which in both cases are localized to transitions immediately surrounding the open conformation. Structural similarities include the triggering of both forms of modulation by the C-terminal lobe of CaM (Peterson et al., 1999; DeMaria et al., 2001; Chaudhuri et al., 2005); and the sensitivity of both forms of regulation to similar structural manipulations within the IQ domain (Zuhlke et al., 1999, 2000; DeMaria et al., 2001) and EF-hand locus (de Leon et al., 1995; Zuhlke and Reuter, 1998; Peterson et al., 2000; Chaudhuri et al., 2001, 2004). Given these correlations, it is tempting to speculate that $Ca_V2.1$ CDF and $Ca_V1.2$ CDI represent structurally analogous mechanisms wherein the polarity of mode switching by Ca^{2+}/CaM has been inverted.

The original human α_{1A} ($\alpha_1$2.1) clone is a gift from Dr. Terry Snutch (University of British Columbia, Vancouver, BC Canada). Some preliminary data were collected by Drs. Tuck W. Soong (National Neuroscience Institute, Singapore) and Carla D. DeMaria (Georgetown University, Washington, DC). We thank Shoji Takahashi for valuable insight in preparation of the manuscript.

This work was supported by National Institutes of Health (NIH) MSTP fellowships (D. Chaudhuri and J.B. Issa), and grants from the NIH (D.T. Yue).

Olaf S. Andersen served as editor.

Submitted: 22 January 2007
Accepted: 20 March 2007

REFERENCES

Abbott, L.F., and W.G. Regehr. 2004. Synaptic computation. *Nature.* 431:796–803.

Aldrich, R.W., and C. Stevens. 1983. Inactivation of open and closed sodium channels determined separately. *Cold Spring Harb. Symp. Quant. Biol.* 48:147–153.

Alseikhan, B.A., C.D. DeMaria, H.M. Colecraft, and D.T. Yue. 2002. Engineered calmodulins reveal the unexpected eminence of Ca^{2+} channel inactivation in controlling heart excitation. *Proc. Natl. Acad. Sci. USA.* 99:17185–17190.

Augustine, G.J., F. Santamaria, and K. Tanaka. 2003. Local calcium signaling in neurons. *Neuron.* 40:331–346.

Borst, J.G., and B. Sakmann. 1998. Facilitation of presynaptic calcium currents in the rat brainstem. *J. Physiol.* 513:149–155.

Borst, J.G., and B. Sakmann. 1999. Depletion of calcium in the synaptic cleft of a calyx-type synapse in the rat brainstem. *J. Physiol.* 521(Pt 1):123–133.

Borst, J.G.G., F. Helmchen, and B. Sakmann. 1995. Pre- and postsynaptic whole-cell recordings in the medial nucleus of the trapezoid body of the rat. *J. Physiol.* 489:825–840.

Brody, D.L., P.G. Patil, J.G. Mulle, T.P. Snutch, and D.T. Yue. 1997. Bursts of action potential waveforms relieve G-protein inhibition of recombinant P/Q-type Ca^{2+} channels in HEK 293 cells. *J. Physiol.* 499:637–644.

Chao, S.H., Y. Suzuki, J.R. Zysk, and W.Y. Cheung. 1984. Activation of calmodulin by various metal cations as a function of ionic radius. *Mol. Pharmacol.* 26:75–82.

Chaudhuri, D., B.A. Alseikhan, S.Y. Chang, T.W. Soong, and D.T. Yue. 2005. Developmental activation of calmodulin-dependent facilitation of cerebellar P-type Ca^{2+} current. *J. Neurosci.* 25:8282–8294.

Chaudhuri, D., S.Y. Chang, C.D. DeMaria, R.S. Alvania, T.W. Soong, and D.T. Yue. 2004. Alternative splicing as a molecular switch for Ca^{2+}/calmodulin-dependent facilitation of P/Q-type Ca^{2+} channels. *J. Neurosci.* 24:6334–6342.

Colecraft, H.M., D.L. Brody, and D.T. Yue. 2001. G-protein inhibition of N- and P/Q-type calcium channels: distinctive elementary mechanisms and their functional impact. *J. Neurosci.* 21:1137–1147.

Colquhoun, D., and A. Hawkes. 1982. On the stochastic properties of bursts of single ion channel openings and of clusters of bursts. *Philos. Trans. R. Soc. Lond. B Biol. Sci.* 300:1–59.

Cuttle, M.F., T. Tsujimoto, I.D. Forsythe, and T. Takahashi. 1998. Facilitation of the presynaptic calcium current at an auditory synapse in rat brainstem. *J. Physiol.* 512:723–729.

de Leon, M., Y. Wang, L. Jones, E. Perez-Reyes, X. Wei, T.W. Soong, T.P. Snutch, and D.T. Yue. 1995. Essential Ca^{2+}-binding motif for Ca^{2+}-sensitive inactivation of L-type Ca^{2+} channels. *Science.* 270:1502–1506.

DeMaria, C.D., T.W. Soong, B.A. Alseikhan, R.S. Alvania, and D.T. Yue. 2001. Calmodulin bifurcates the local Ca^{2+} signal that modulates P/Q-type Ca^{2+} channels. *Nature.* 411:484–489.

Dhallan, R.S., K.W. Yau, K.A. Schrader, and R.R. Reed. 1990. Primary structure and functional expression of a cyclic nucleotide-activated channel from olfactory neurons. *Nature.* 347:184–187.

Dodge, F.A., Jr., and R. Rahamimoff. 1967. Co-operative action a calcium ions in transmitter release at the neuromuscular junction. *J. Physiol.* 193:419–432.

Dove, L.S., L.C. Abbott, and W.H. Griffith. 1998. Whole-cell and single-channel analysis of P-type calcium currents in cerebellar Purkinje cells of leaner mutant mice. *J. Neurosci.* 18:7687–7699.

Dunlap, K., J.I. Luebke, and T.J. Turner. 1995. Exocytotic Ca^{2+} channels in mammalian central neurons. *Trends Neurosci.* 18:89–98.

Erickson, M.G., B.A. Alseikhan, B.Z. Peterson, and D.T. Yue. 2001. Preassociation of calmodulin with voltage-gated Ca^{2+} channels revealed by FRET in single living cells. *Neuron.* 31:973–985.

Evans, R.M., and G.W. Zamponi. 2006. Presynaptic Ca^{2+} channels–integration centers for neuronal signaling pathways. *Trends Neurosci.* 29:617–624.

Fellin, T., S. Luvisetto, M. Spagnolo, and D. Pietrobon. 2004. Modal gating of human CaV2.1 (P/Q-type) calcium channels: II. The b mode and reversible uncoupling of inactivation. *J. Gen. Physiol.* 124:463–474.

Hamill, O.P., A. Marty, E. Neher, B. Sakmann, and F.J. Sigworth. 1981. Improved patch-clamp techniques for high-resolution current recording from cells and cell-free membrane patches. *Pflugers Arch.* 391:85–100.

Hans, M., S. Luvisetto, M.E. Williams, M. Spagnolo, A. Urrutia, A. Tottene, P.F. Brust, E.C. Johnson, M.M. Harpold, K.A. Stauderman, and D. Pietrobon. 1999. Functional consequences of mutations in the human α1A calcium channel subunit linked to familial hemiplegic migraine. *J. Neurosci.* 19:1610–1619.

Horn, R. 1991. Estimating the number of channels in patch recordings. *Biophys. J.* 60:433–439.

Imredy, J.P., and D.T. Yue. 1992. Submicroscopic Ca^{2+} diffusion mediates inhibitory coupling between individual Ca^{2+} channels. *Neuron.* 9:197–207.

Imredy, J.P., and D.T. Yue. 1994. Mechanism of Ca^{2+}-sensitive inactivation of L-type Ca^{2+} channels. *Neuron.* 12:1301–1318.

Jones, L.P., C.D. DeMaria, and D.T. Yue. 1999. N-type calcium channel inactivation probed by gating-current analysis. *Biophys. J.* 76:2530–2552.

Kink, J.A., M.E. Maley, R.R. Preston, K.Y. Ling, M.A. Wallen-Friedman, Y. Saimi, and C. Kung. 1990. Mutations in paramecium calmodulin indicate functional differences between the C-terminal and N-terminal lobes in vivo. *Cell.* 62:165–174.

Lee, A., T. Scheuer, and W.A. Catterall. 2000. Ca^{2+}/calmodulin-dependent facilitation and inactivation of P/Q-type Ca^{2+} channels. *J. Neurosci.* 20:6830–6838.

Lee, A., S.T. Wong, D. Gallagher, B. Li, D.R. Storm, T. Scheuer, and W.A. Catterall. 1999. Ca^{2+}/calmodulin binds to and modulates P/Q-type calcium channels. *Nature.* 399:155–159.

Lee, A., H. Zhou, T. Scheuer, and W.A. Catterall. 2003. Molecular determinants of Ca^{2+}/calmodulin-dependent regulation of Ca(v)2.1 channels. *Proc. Natl. Acad. Sci. USA.* 100:16059–16064.

Liang, H., C.D. DeMaria, M.G. Erickson, M.X. Mori, B.A. Alseikhan, and D.T. Yue. 2003. Unified mechanisms of Ca^{2+} regulation across the Ca^{2+} channel family. *Neuron.* 39:951–960.

Lipscombe, D., and A.J. Castiglioni. 2003. Alternative splicing in voltage-gated calcium channels. *In* Calcium Channel Pharmacology. S.I. McDonough, editor. Springer-Verlag, New York. 369–410.

Lipscombe, D., J.Q. Pan, and A.C. Gray. 2002. Functional diversity in neuronal voltage-gated calcium channels by alternative splicing of Ca(v)alpha1. *Mol. Neurobiol.* 26:21–44.

Luvisetto, S., T. Fellin, M. Spagnolo, B. Hivert, P.F. Brust, M.M. Harpold, K.A. Stauderman, M.E. Williams, and D. Pietrobon. 2004. Modal gating of human CaV2.1 (P/Q-type) calcium channels: I. The slow and the fast gating modes and their modulation by beta subunits. *J. Gen. Physiol.* 124:445–461.

Park, D., and K. Dunlap. 1998. Dynamic regulation of calcium influx by G-proteins, action potential waveform, and neuronal firing frequency. *J. Neurosci.* 18:6757–6766.

Patil, P.G., D.L. Brody, and D.T. Yue. 1998. Preferential closed-state inactivation of neuronal calcium channels. *Neuron.* 20:1027–1038.

Patil, P.G., M. de Leon, R.R. Reed, S. Dubel, T.P. Snutch, and D.T. Yue. 1996. Elementary events underlying voltage-dependent G-protein inhibition of N-type calcium channels. *Biophys. J.* 71:2509–2521.

Perez-Reyes, E., A. Castellano, H.S. Kim, P. Bertrand, E. Baggstrom, A.E. Lacerda, X.Y. Wei, and L. Birnbaumer. 1992. Cloning and expression of a cardiac/brain β subunit of the L-type calcium channel. *J. Biol. Chem.* 267:1792–1797.

Peterson, B.Z., C.D. DeMaria, J.P. Adelman, and D.T. Yue. 1999. Calmodulin is the Ca^{2+} sensor for Ca^{2+}-dependent inactivation of L-type calcium channels. *Neuron.* 22:549–558.

Peterson, B.Z., J.S. Lee, J.G. Mulle, Y. Wang, M. de Leon, and D.T. Yue. 2000. Critical determinants of Ca^{2+}-dependent inactivation within an EF-hand motif of L-type Ca^{2+} channels. *Biophys. J.* 78:1906–1920.

Sabatini, B.L., and W.G. Regehr. 1997. Control of neurotransmitter release by presynaptic waveform at the granule cell to Purkinje cell synapse. *J. Neurosci.* 17:3425–3435.

Sigworth, F.J. 1981. Covariance of nonstationary sodium current fluctuations at the node of Ranvier. *Biophys. J.* 34:111–133.

Soong, T.W., C.D. DeMaria, R.S. Alvania, L.S. Zweifel, M.C. Liang, S. Mittman, W.S. Agnew, and D.T. Yue. 2002. Systematic identification of splice variants in human P/Q-type channel alpha1(2.1) subunits: implications for current density and Ca^{2+}-dependent inactivation. *J. Neurosci.* 22:10142–10152.

Stotz, S.C., W. Barr, J.E. McRory, L. Chen, S.E. Jarvis, and G.W. Zamponi. 2004. Several structural domains contribute to the regulation of N-type calcium channel inactivation by the β3 subunit. *J. Biol. Chem.* 279:3793–3800.

Tomlinson, W.J., A. Stea, E. Bourinet, P. Charnet, J. Nargeot, and T.P. Snutch. 1993. Functional properties of a neuronal class C L-type calcium channel. *Neuropharmacology.* 32:1117–1126.

Tottene, A., T. Fellin, S. Pagnutti, S. Luvisetto, J. Striessnig, C. Fletcher, and D. Pietrobon. 2002. Familial hemiplegic migraine mutations increase Ca^{2+} influx through single human CaV2.1 channels and decrease maximal CaV2.1 current density in neurons. *Proc. Natl. Acad. Sci. USA.* 99:13284–13289.

Tottene, A., F. Pivotto, T. Fellin, T. Cesetti, A.M. van den Maagdenberg, and D. Pietrobon. 2005. Specific kinetic alterations of human CaV2.1 calcium channels produced by mutation S218L causing familial hemiplegic migraine and delayed cerebral edema and coma after minor head trauma. *J. Biol. Chem.* 280:17678–17686.

Tsodyks, M., K. Pawelzik, and H. Markram. 1998. Neural networks with dynamic synapses. *Neural Comput.* 10:821–835.

Tsodyks, M.V., and H. Markram. 1997. The neural code between neocortical pyramidal neurons depends on neurotransmitter release probability. *Proc. Natl. Acad. Sci. USA.* 94:719–723.

Wheeler, D.B., A. Randall, and R.W. Tsien. 1994. Roles of N-type and Q-type Ca^{2+} channels in supporting hippocampal synaptic transmission. *Science.* 264:107–111.

Wheeler, D.B., and R.W. Tsien. 1999. Voltage-gated calcium channels. *In* Calcium as a Cellular Regulator. E. Carafoli and C. Lee, editors. Oxford University Press, New York. 171–199.

Xu, J., and L.G. Wu. 2005. The decrease in the presynaptic calcium current is a major cause of short-term depression at a calyx-type synapse. *Neuron.* 46:633–645.

Yang, P.S., B.A. Alseikhan, H. Hiel, L. Grant, M.X. Mori, W. Yang, P.A. Fuchs, and D.T. Yue. 2006. Switching of Ca^{2+}-dependent inactivation of Ca(v)1.3 channels by calcium binding proteins of auditory hair cells. *J. Neurosci.* 26:10677–10689.

Yue, D.T., P.H. Backx, and J.P. Imredy. 1990. Calcium-sensitive inactivation in the gating of single calcium channels. *Science.* 250:1735–1738.

Zucker, R.S., and W.G. Regehr. 2002. Short-term synaptic plasticity. *Annu. Rev. Physiol.* 64:355–405.

Zuhlke, R.D., G.S. Pitt, K. Deisseroth, R.W. Tsien, and H. Reuter. 1999. Calmodulin supports both inactivation and facilitation of L-type calcium channels. *Nature.* 399:159–162.

Zuhlke, R.D., G.S. Pitt, R.W. Tsien, and H. Reuter. 2000. Ca^{2+}-sensitive inactivation and facilitation of L-type Ca^{2+} channels both depend on specific amino acid residues in a consensus calmodulin-binding motif in the α1C subunit. *J. Biol. Chem.* 275:21121–21129.

Zuhlke, R.D., and H. Reuter. 1998. Ca^{2+}-sensitive inactivation of L-type Ca^{2+} channels depends on multiple cytoplasmic amino acid sequences of the α1C subunit. *Proc. Natl. Acad. Sci. USA.* 95:3287–3294.